Effect of Reactant Pressure on Proton Exchange Membrane Fuel Cell Performance

Phillip J. Smith, William R. Bennett, Ian J. Jakupca, and Ryan P. Gilligan
Glenn Research Center, Cleveland, Ohio

Lawrence G. Edwards
Vantage Partners, LLC, Brook Park, Ohio

NASA STI Program . . . in Profile

Since its founding, NASA has been dedicated to the advancement of aeronautics and space science. The NASA Scientific and Technical Information (STI) Program plays a key part in helping NASA maintain this important role.

The NASA STI Program operates under the auspices of the Agency Chief Information Officer. It collects, organizes, provides for archiving, and disseminates NASA's STI. The NASA STI Program provides access to the NASA Technical Report Server—Registered (NTRS Reg) and NASA Technical Report Server—Public (NTRS) thus providing one of the largest collections of aeronautical and space science STI in the world. Results are published in both non-NASA channels and by NASA in the NASA STI Report Series, which includes the following report types:

- TECHNICAL PUBLICATION. Reports of completed research or a major significant phase of research that present the results of NASA programs and include extensive data or theoretical analysis. Includes compilations of significant scientific and technical data and information deemed to be of continuing reference value. NASA counter-part of peer-reviewed formal professional papers, but has less stringent limitations on manuscript length and extent of graphic presentations.

- TECHNICAL MEMORANDUM. Scientific and technical findings that are preliminary or of specialized interest, e.g., "quick-release" reports, working papers, and bibliographies that contain minimal annotation. Does not contain extensive analysis.

- CONTRACTOR REPORT. Scientific and technical findings by NASA-sponsored contractors and grantees.

- CONFERENCE PUBLICATION. Collected papers from scientific and technical conferences, symposia, seminars, or other meetings sponsored or co-sponsored by NASA.

- SPECIAL PUBLICATION. Scientific, technical, or historical information from NASA programs, projects, and missions, often concerned with subjects having substantial public interest.

- TECHNICAL TRANSLATION. English-language translations of foreign scientific and technical material pertinent to NASA's mission.

For more information about the NASA STI program, see the following:

- Access the NASA STI program home page at http://www.sti.nasa.gov

- E-mail your question to help@sti.nasa.gov

- Fax your question to the NASA STI Information Desk at 757-864-6500

- Telephone the NASA STI Information Desk at 757-864-9658

- Write to:
  NASA STI Program
  Mail Stop 148
  NASA Langley Research Center
  Hampton, VA 23681-2199

Effect of Reactant Pressure on Proton Exchange Membrane Fuel Cell Performance

Phillip J. Smith, William R. Bennett, Ian J. Jakupca, and Ryan P. Gilligan
Glenn Research Center, Cleveland, Ohio

Lawrence G. Edwards
Vantage Partners, LLC, Brook Park, Ohio

National Aeronautics and
Space Administration

Glenn Research Center
Cleveland, Ohio 44135

Level of Review: This material has been technically reviewed by expert reviewer(s).

Contents

Effect of Reactant Pressure on Proton Exchange Membrane Fuel Cell Performance

Phillip J. Smith, William R. Bennett, Ian J. Jakupca, and Ryan P. Gilligan
National Aeronautics and Space Administration
Glenn Research Center
Cleveland, Ohio 44135

Lawrence G. Edwards
Vantage Partners, LLC
Brook Park, Ohio 44142

Summary

It is an objective of NASA to return to the Moon and to create sustained lunar operations. Since many applicable lander and upper-stage vehicles utilize cryogenic hydrogen and oxygen propellants, it is appealing to incorporate fuel cells into potential mission concepts. A fuel cell could generate electricity, heat, and water from the residual hydrogen and oxygen propellants. Such a concept depends on the capability of the fuel cell to utilize dry, propellant-grade reactants at reduced pressures compared with typical fuel cell operating conditions. This report describes a NASA evaluation of two passive water removal, non-flow-through proton exchange membrane fuel cells: a 12-cell stack with 50 cm^2 active area and a 7-cell stack with 150 cm^2 active area. Both stacks operated on research-grade hydrogen and oxygen reactants supplied at pressures ranging from 138 kPa (20 psia) up to the 310- to 331-kPa (45- to 48-psia) design operating point, reliably supporting current densities of at least 450 mA/cm^2 at reduced pressures. Polarization curves, fitted with a semi-empirical equation for overpotential, show an increase in effective ohmic resistance and decreases in reversible cell potential, hydrogen crossover current, and Tafel slope when operating at lower pressures, which resulted in a reduction in cell potential at all current densities. Fitted parameters are compared with published values and rationalized with first-principles explanations.

1.0 Introduction

Current NASA plans for space exploration include long-term Lunar Gateway and surface missions (Ref. 1). Since it is considerably more expensive to reach the lunar surface than to simply transport to low Earth orbit, there is a sustained focus on minimizing launch weight when developing the technologies required to implement these missions. Consequently, there is considerable motivation to identify such technologies that are compatible with the delivery system, and fuel cells present an enticing opportunity when propellants are hydrogen and oxygen. Reactant storage mass and volume frequently comprise the majority of the total mass and volume for fuel cell systems. Large cost savings are possible when replacing a dedicated fuel cell reactant storage system with excess propellant carried by a descent vehicle to provide a safety margin during flight.

In 2007, an Altair lunar lander module mission concept considered residual hydrogen and oxygen for application as a fuel cell reactant supply in a lunar lander mission (Refs. 2 and 3). Estimated residual propellant was 3 percent of the initial quantity (Ref. 2). For the described nominal mission case, 130 kg hydrogen and 706 kg oxygen remain unused. At an energy conversion ratio of 2.2 kWh/kg water, equivalent to 60 percent of theoretical available energy, and assuming complete utilization of the scavenged propellant with oxygen as the limiting reactant, a fuel cell generates 1,746 kWh of electrical energy and 794 kg of water from such a reactant quantity. Since this propellant is required regardless of the inclusion of fuel cells, it may replace a fuel-cell-specific reactant storage system. The question remains whether modern aerospace flight fuel cells are capable of efficiently utilizing these relatively impure propellants at these relatively low pressures.

Altair lander tank pressures range from 62 to 310 kPa (9 to 45 psia) oxygen and 117 to 228 kPa (17 to 33 psia) hydrogen. This generally aligns well with typical operating pressure levels of PEM fuel cells, although the design pressures are slightly higher at 310 to 345 kPa (45 to 50 psia). It is common to operate terrestrial hydrogen-air fuel cells with blowers to circulate and pressurize reactant, but these active ancillary components reduce overall efficiency and increase system complexity and mass. Preferred aerospace fuel cell systems incorporate passive components for improved system-level simplicity, specific energy, and energy density (Ref. 4). Thus, to realize the full power production potential for a fuel cell and residual propellant system, the fuel cell system must be designed to perform at lower than optimal pressures and minimize the reduced capability that results.

There are many methods for ex situ characterization of fuel cell components, but fundamental properties are not necessarily

simple to equate to performance in real fuel cell operating conditions. The current work involves in situ evaluation of various performance parameters and enables later modeling and performance predictions for the design.

Abbreviations and symbols used in this report are listed in Appendix A.

2.0   Experimental

Two passive water removal non-flow-through (NFT) proton exchange membrane (PEM) fuel cell stacks were utilized for this testing. One stack consisted of 12 cells with 50 cm^2 active area and Nafion^{TM} N117 (The Chemours Company FC, LLC) membranes. The other was a 7-cell stack with 150 cm^2 active area and the same membrane. Prior to pressure sensitivity testing, the two fuel cells used in this study were also exposed to launch vibration sensitivity testing while in a pressurized, but inert, nonoperational state in a variety of stack orientations with respect to gravity (i.e., operational positions). No significant performance changes were found as a result of those evaluations (Ref. 5). The 12-cell stack was also used for a reactant impurity sensitivity study (Ref. 6). The stack proved capable of operating with up to 30 percent helium in the reactant supply. It is of interest to continue addressing fuel cell performance issues likely to be encountered in a flight application that differs from standard laboratory operating conditions.

The testing was performed at the NASA Glenn Research Center on a NASA-developed NFT PEM fuel cell Common Test Bed (CTB). There is an extensive history for using the CTB for fuel cell testing (Refs. 5 to 8). This CTB integrates manual and automated control of operating temperatures, pressures, and flow rates as well as enables remote operator control through a LabVIEW (National Instruments Corp.) program and an associated National Instruments CompactRIO™ controller. Current load was drawn from the stacks by a programmable electronic load. A 2-h load profile, preceded and followed by current sweeps as shown in Figure 1, was utilized for both stacks at each pressure.

It is possible to use an empirical fit relating current load to cell potential to quantify physical phenomena such as the hydrogen crossover current (Refs. 9 and 10). Best-fit lines were generated using an equation format developed and employed by Hao et al. (Ref. 11), consisting of only three fitted parameters. This semi-empirical equation relates current density i (mA/cm^2) to cell potential E (V) by

$$E = E_{OCV} - b * \log\left(\frac{i + i_c}{i_c}\right) - R_\Omega * i \qquad (1)$$

where E_{OCV} is the observed open-circuit voltage (potential), b is the fitted Tafel slope, i_c is the fitted parasitic crossover current density, and R_Ω is the fitted ohmic resistance. This equation achieves a high quality of fit by using terms that have physical significance and a minimum number of fitted parameters. In previous versions, instead of E_{OCV}, the first equation term is often a fitted parameter, E_0, which encompasses reversible potential that is challenging to accurately determine and leads to wide potential variability for other fit parameters. Many equations using logarithmic terms do not enable calculation of a cell potential value at 0 mA/cm^2. The current version incorporates parasitic crossover in a manner that functions at no current load. Microsoft Excel Solver was used to vary the three fitted parameters in order to minimize the sum of squared residuals for the experimentally recorded and calculated cell potentials.
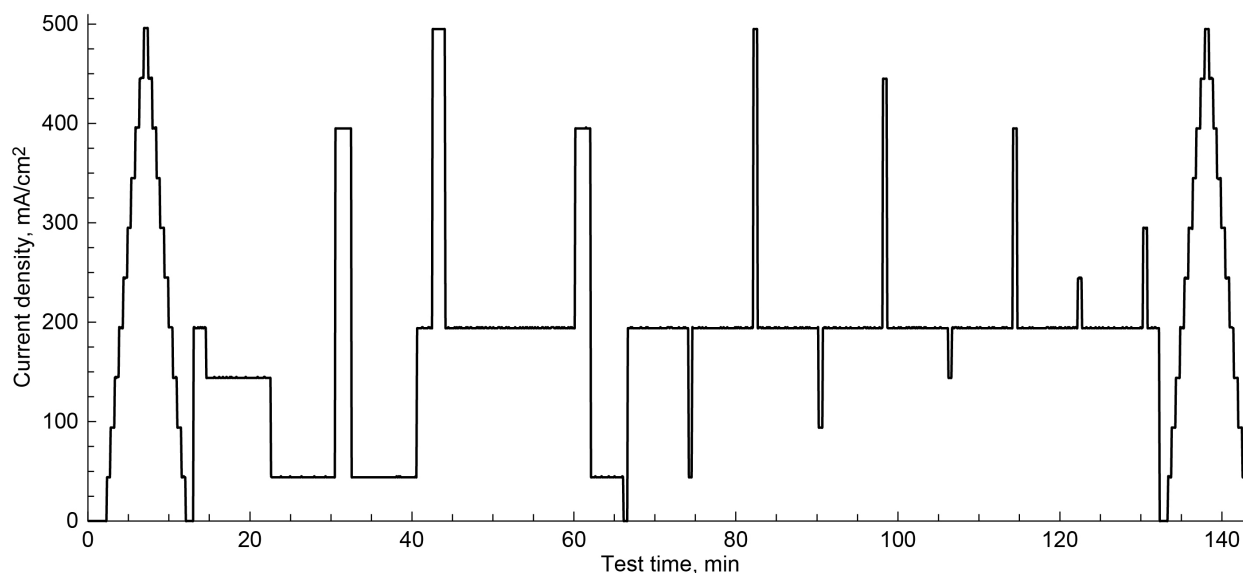

Figure 1.—Fuel cell load profile used for testing.

The NFT PEM stacks were not operated at high enough current densities to obtain information on mass-transport limitations, so a mass transport term was not included. This is effectively an assumption that the studied current densities are sufficiently lower than the true limiting current density so that reaction site gas pressure is uniform and equal to the supply pressure (Ref. 12).

The effect of pressure on the thermodynamic voltage of the fuel cell can be predicted using the Nernst equation. For the reaction $H_2 + \frac{1}{2} O_2 \rightarrow H_2O$, the Nernst relationship can be used to adjust the cell potential in Equation (1) to account for various operational pressures by

$$E = E^0 + \frac{RT_0}{2F} \ln\left(\frac{p_{H_2} p_{O_2}^{1/2}}{a_{H_2O}} \right) \qquad (2)$$

where E^0 is the standard cell potential, R is the ideal gas constant, F is the Faraday constant, T_0 is absolute temperature (same conditions as E^0), p_{H_2} is hydrogen partial pressure, p_{O_2} is oxygen partial pressure, and a_{H_2O} is the activity of water (Ref. 13). Assuming pure reactants at balanced pressure p (atm) when $p = p_{H_2} = p_{O_2}$ and activity of water equal to 1, then differentiating with respect to pressure produces

$$\frac{\partial E}{\partial p} = \frac{3RT_0}{4Fp} \qquad (3)$$

which enables calculation of the theoretical effect of pressure on the cell potential. Equation (2) can also be used to calculate the resultant change in cell potential ΔE as a consequence of varying reactant pressures through

$$\Delta E = E_{adj} - E_{ref} = \frac{3RT_0}{4F} \ln\left(\frac{p_{adj}}{p_{ref}} \right) \qquad (4)$$

where "adj" indicates the adjusted condition to be evaluated and "ref" represents values at the known initial reference condition. For this analysis, stacks were assumed to have a uniform 70 °C

internal cell temperature. The actual measured coolant stack outlet temperature was controlled to 60 °C throughout all testing. These Nernst cell potential changes were calculated for each reduced pressure condition in reference to the highest tested pressure condition. Then, the Nernst adjusted cell potentials were compared to the actual cell potential performance at the reduced pressures.

For evaluation of the fitted R_Ω, an empirical fit equation (Ref. 14) was used to calculate Nafion™ conductivity σ such that

$$\sigma = \left(0.6877 + a_{H_2O} \right)^3 \exp\left(\frac{-10440 a_{H_2O}^{-1/4}}{RT_0} \right) \qquad (5)$$

From conductivity, the calculated membrane resistance R_{calc} is

$$R_{calc} = \frac{l}{\sigma} \qquad (6)$$

where l is the membrane thickness.

2.1 Measurement Uncertainties

Empirical modeling relies on quality experimental measurements, since any systemic errors carry forward into the equation fit. Table I provides the measurement uncertainties for pressure, temperature, voltage (potential difference), and current measurements used for this work. All are estimated from instrumentation and signal conditioning system specifications, with lab temperature variability effects included over the ambient temperature range of 25±5 °C. Instruments were user calibrated against known calibrated standards.

With the utilized instrumentation setup, fuel cell stack total voltage uncertainty is reduced by measuring all cells individually, rather than measuring one voltage across all power-producing cells. For the 7-cell stack, the worst-case summed error is ±19 mV and the root-sum-square error is ±7 mV. For the 12-cell stack, the worst-case summed error is ±32 mV and the root-sum-square error is ±9 mV.

TABLE I.—INSTRUMENT MEASUREMENT UNCERTAINTY

Measurement	Instrument	Maximum reading	Uncertainty[a]
Current	Datel 0.25-mΩ shunt	200 Adc	±0.065 Adc or ±0.3%[b]
Pressure	Setra Model 225 transducers[c]	345 kPa (50 psi)	±1.1 kPa (±0.16 psi)
Temperature	Omega Type T thermocouple probes[d]	125 mVdc	±1.5 °C
Voltage	National Instruments NI-9219 signal conditioner	15 Vdc	±2.7 mVdc

[a]If two options are presented, whichever is greater applies.

[b]Percentage of current reading.

[c]Measured with National Instruments NI-9205 signal conditioner.

[d]Measured with National Instruments NI-9219 signal conditioner.

TABLE II.—TWELVE-CELL PEM FUEL CELL STACK
AVERAGE OBSERVED OPEN-CIRCUIT POTENTIAL
AND FITTED PARAMETERS FOR EQUATION (1)[a]

Reactant pressure		Open-circuit potential, E_{OCV}, V	Tafel slope,[b] b, mV/dec	Crossover current density, i_c, 10^3 mA/cm^2	Ohmic resistance, R_Ω, $\Omega \cdot$cm^2
kPa	psi				
138	20	1.01	37.9	3.94	0.358
172	25	1.02	40.0	3.60	0.321
331	48	1.06	44.4	3.19	0.308

[a] $E = E_{OCV} - b * \log\left(\dfrac{i + i_c}{i_c}\right) - R_\Omega * i$.
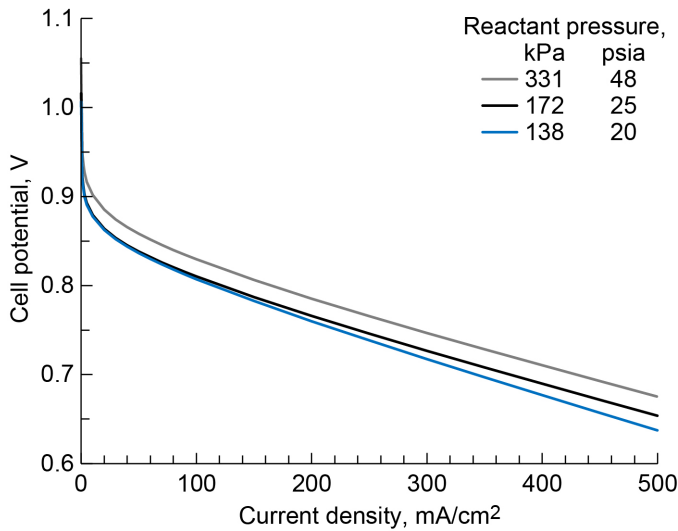
[b]In millivolts per decade.

Figure 2.—Twelve-cell PEM fuel cell stack polarization curves at different reactant pressures.

3.0　Results

Table II lists the three Equation (1) empirical fitted parameters for operation of the NFT PEM 12-cell stack at the three tested operational pressures, and Figure 2 shows the calculated cell potentials as a function of current density. There are minimal performance differences between the 138 and 172 kPa (20 and 25 psia) cases. Best equation fits are achieved with i_c near 0 for each pressure level. Operating at 331 kPa (48 psia) increases E_{OCV} by more than 40 mV and reduces R_Ω by about 14 percent, compared to operating at 138 kPa (20 psia). This results in a consistent trend of greater power production at higher pressure for a given current density. In the load profile, supplied with 138 kPa (20 psia) compared to 331 kPa (48 psia), the stack produces 2.7 percent less power at 100 mA/cm^2 and 5.6 percent less power at 500 mA/cm^2.

TABLE III.—SEVEN-CELL PEM FUEL CELL STACK
AVERAGE OBSERVED OPEN-CIRCUIT POTENTIAL
AND FITTED PARAMETERS FOR EQUATION (1)[a]

Reactant pressure		Open-circuit potential, E_{OCV}, V	Tafel slope,[b] b, mV/dec	Crossover current density, i_c, mA/cm^2	Ohmic resistance, R_Ω, $\Omega \cdot$cm^2
kPa	psi				
138	20	1.03	49.4	0.192	0.469
172	25	1.03	51.4	0.235	0.447
207	30	1.04	56.2	0.392	0.423
310	45	1.07	92.2	2.11	0.331

[a] $E = E_{OCV} - b * \log\left(\dfrac{i + i_c}{i_c}\right) - R_\Omega * i$.
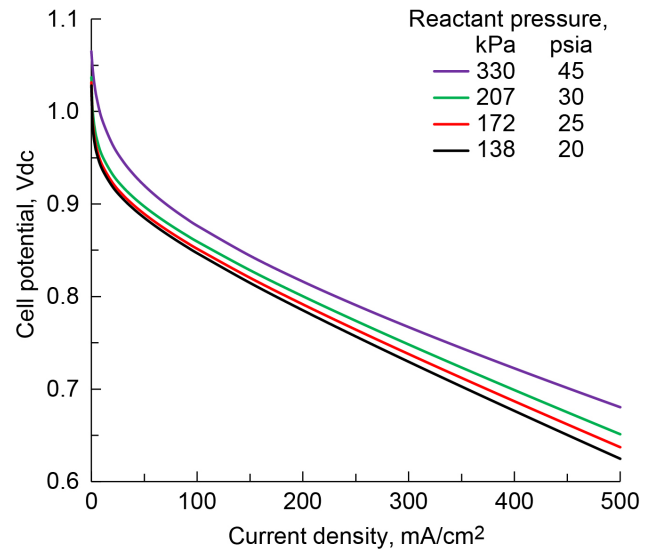
[b]In millivolts per decade.

Figure 3.—Seven-cell PEM fuel cell stack fitted polarization curves at different reactant pressures.

Table III provides the Equation (1) empirical fitted parameters for operation of the NFT PEM 7-cell stack at the four tested operational pressures, and Figure 3 displays the calculated cell potentials as a function of current density. For this stack, higher reactant pressure increases E_{OCV}, b, and i_c while decreasing R_Ω. At 500 mA/cm^2, the stack produces 8.2 percent less power at 138 kPa (20 psia) compared to at 310 kPa (45 psia). To enable fit quality evaluation for both stacks, calculated cell potentials as a function of current density and raw data points are provided in Appendix B.

For each stack, the observed and fitted parameters are plotted versus pressure in Figure 4. The 7-cell stack performance appears more influenced by pressure and less linear in response than the 12-cell stack. The magnitude and slope for each fitted parameter are greater for the 7-cell values for all pressure levels.
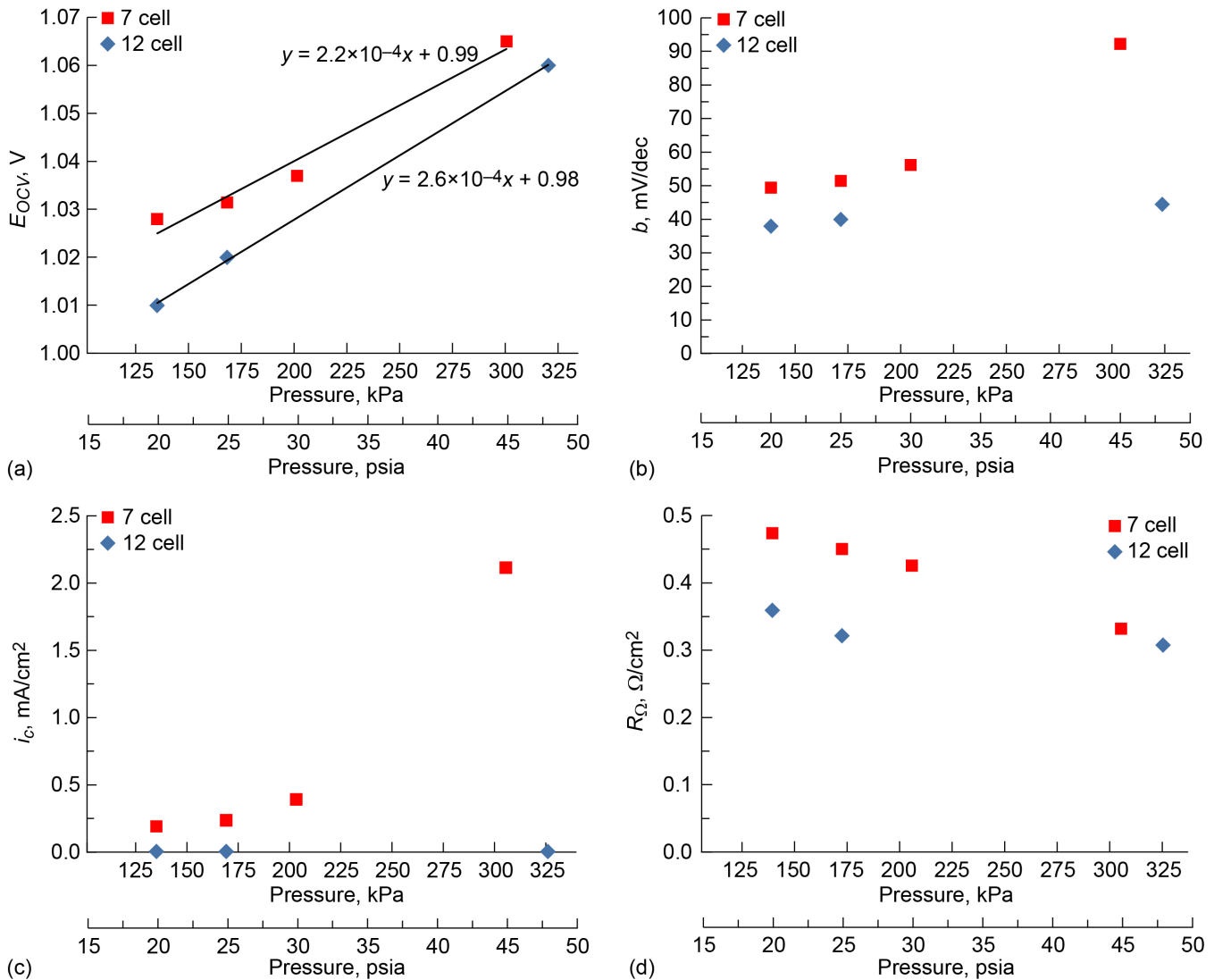
Figure 4.—Equation (1) parameters as a function of pressure for 7- and 12-cell PEM fuel cell stacks. (a) Open-circuit potential, E_{OCV}; line fits evaluated for pressures in kilopascals. (b) Tafel slope, b. (c) Crossover current density, i_c. (d) Ohmic resistance, R_Ω.

To highlight the possible efficiency improvements from operating at increased pressure, Figure 5 shows the current density required to achieve certain power densities for each tested fuel cell stack operating condition. To produce 0.3 W/cm^2 (equivalent to 315 W for the 7-cell stack and 180 W for the 12-cell stack), the current load for the 7-cell stack is 11 percent greater at the lowest tested pressure than at the highest one; likewise, the current load for the 12-cell stack is 7.1 percent greater at the lowest tested pressure than at the highest one. To produce 0.05 W/cm^2 (equivalent to 52 W for the 7-cell stack and 30 W for the 12-cell stack), the current load for the 7-cell is 4.5 percent greater at the lowest tested pressure than at the highest one; and similarly the current load for the 12-cell is 2.9 percent greater at the lowest tested pressure than at the highest one. Thus, the trends appear similar for both stacks: there is an efficiency benefit to operating at higher pressure for any power level, though there is less improvement at lower power levels.
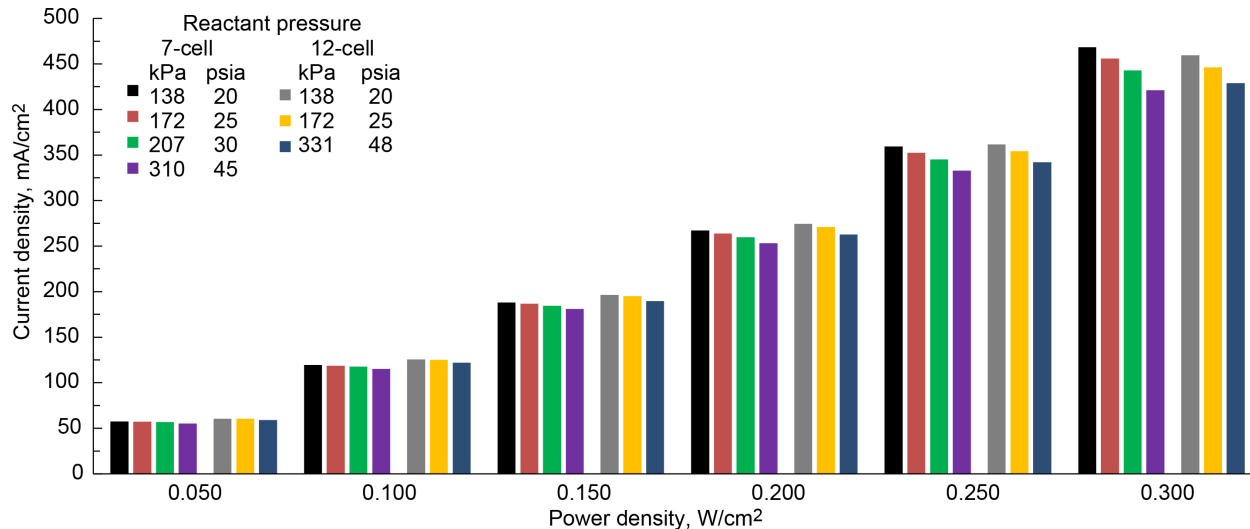
Figure 5.—Current densities needed to achieve a given power density level for the 7- and 12-cell PEM fuel cell stacks at each tested operational pressure condition.

3.1 Open Circuit Potential E_{OCV} and Crossover Current i_c Discussion

The observed E_{OCV} values are in line with existing reporting that open-circuit potential should range from 0.99 to 1.03 V at 70 °C and 303 kPa (44 psia) (Ref. 9). The difference between the practical cell potentials versus the theoretical ideal potential is attributed exclusively to hydrogen crossover and the resulting oxygen reduction reaction overpotential at the cathode. The importance of hydrogen crossover makes it worthwhile to include in the model equation. A 1 to 10 mA/cm^2 internal current density leads to an estimated cathode overpotential equivalent to experimental obvervations (Ref. 9). The magnitude of this internal current is one indicator of membrane health and is expected to increase over long operational durations (Ref. 10).

For Nafion™ N117 membranes, which is the membrane utilized in the construction of both stacks in this evaluation, at atmospheric pressure and temperature ranging from 60 to 80 °C, hydrogen crossover current density has been observed to range from 0.12 to 0.24 mA/cm^2 (Ref. 10). Previous NASA testing of a 7-cell 150-cm^2 NFT PEM stack experimentally determined the hydrogen crossover current density to be 1 mA/cm^2 (Ref. 8). These are within the range of what is found here for the 7-cell fitted values (Figure 4(c)). The 12-cell fitted values are much smaller, more likely because of fitting limitations of insufficient low-current-density data rather than physical factors. However, in empirical modeling of relatively thick membranes such as Nafion™ N117, crossover has in the past been deemed inconsequential (Ref. 15). The low fitted 12-cell crossover current aligns with such a theory. This appears wholly beneficial in practice, but the authors point out that the likelihood of anode-side drying and cathode-side flooding increases when operating thicker membranes at higher current densities due to relative internal water transport rates. Backdiffusion of water may occur at an insufficient rate to counteract electro-osmotic drag. In thinner membranes, gas crossover levels are more impacted by inputs such as temperature and may actually perform worse at elevated temperature.

There are several additional factors that influence the crossover rate. Higher temperature, pressure, humidity, and operational hours increase hydrogen crossover (Refs. 10 and 16). It should be noted that higher pressure here means only higher hydrogen pressure, as cathode-side pressure was observed to not influence hydrogen crossover (Ref. 17). These resultant effects, in absolute terms, are in fractions of a mA/cm^2 and require many polarization curve data points in the 0.1 to 1 mA/cm^2 range to accurately resolve the crossover current. More crossover equates to more wear, due to hydrogen peroxide formation, which is evidenced by membrane thinning, and thinner membranes exhibit more crossover. It is a positive feedback loop that increases degradation rate over time. For best reliability, hydrogen crossover should be minimized. With an appropriate low-current-density-focused polarization curve, hydrogen crossover can be quantified and monitored over time.

Average cell potential increases with the cathode pressure specifically, in a hydrogen-air stack, because of the greater reactant concentration at higher pressure, which decreases the activation and concentration overpotentials in PEM fuel cells (Ref. 18). Stack output power, which also represents the stack efficiency, increases almost linearly with the stack inlet pressure (Ref. 18). Srinivasan relates pressure to concentration overpotential using a pore model and fundamentals (Ref. 12). Activation and concentration overpotential are dominant factors.

TABLE IV.—COMPUTED NERNST EQUATION
DERIVATIVES[a] FOR E VERSUS p

p		dE/dp	
kPa	psi	10^5 V/kPa	10^4 V/psi
103	15	22	15
138	20	16	11
172	25	13	8.9
207	30	11	7.4
310	45	7.1	4.9

[a]From Equation (3), $\partial E/\partial p = 3RT_0/4Fp$, where E is cell potential, p is reactant pressure, R is the ideal gas constant, T_0 is absolute temperature, and F is the Faraday constant.

These characterize fundamental reaction steps that are slowed because of uneven current distributions throughout the electrode surface. Uniform current distribution, as generated in a pore, is more likely to result when reactant concentration increases or the reactant is able to more easily diffuse through a membrane. Current distribution may also influence observed membrane resistance.

To compare with the observed open circuit potentials, potential derivatives computed from the Nernst equation with Equation (3) are listed in Table IV. The derivatives are similar in magnitude to the equation slopes presented in Figure 4(a).

The Equation (4) E_{OCV} Nernst adjustment cannot fully account for the full performance decrement due to reduced operating pressure at any current density. As presented in Figure 6, the more the pressure changes relative to the reference condition (310 kPa), the more the Nernst equation overpredicts cell potential compared with the observed values at any current density. A Nernst adjustment alone is also not able to accommodate all cell performance losses that change in magnitude due to pressure and current density variance. Therefore, if one develops an empirical fit equation based on operational data at a certain reactant supply pressure, the difference in modeled performance at another pressure should be assumed to be greater than that predicted by Equation (4). As is discussed later in Section 3.5, pressure inside the gas cavities is lower than the supply pressure at nonzero current, so the overprediction is expected at higher current loads.

3.2 Tafel Slope b Discussion

The 12-cell fitted Tafel slopes are around 40 mV/dec (dec is decade), and the 7-cell stack exhibited more variability, ranging from 49 to 92 mV/dec. First, it should be noted that the fitted Tafel slope values represent both hydrogen and oxygen half-cell reactions, whereas the Tafel equation is usually applied to individual electrodes. The format of Equation (1) does not
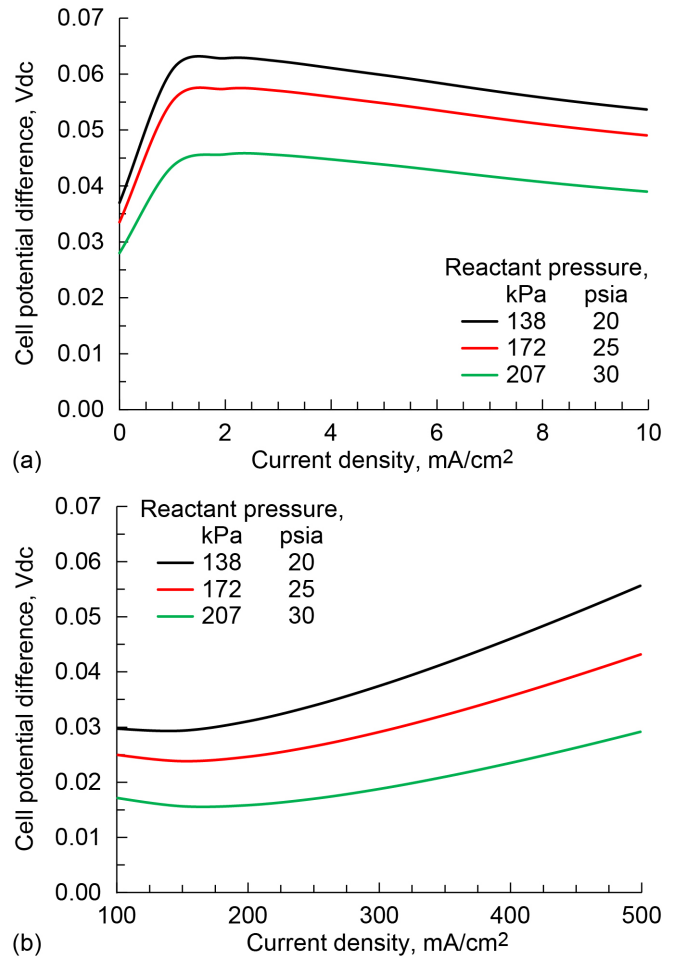

(a)

(b)

Figure 6.—Nernst equation cell potential overprediction compared to actual 7-cell PEM fuel cell stack performance as current density varies. Overprediction is calculated by taking difference in cell potentials calculated with Equation (1) at specified reactant pressure and again at 310 kPa and comparing result with Nernst cell potential change calculated using Equation (4). (a) Current density ranging from 0 to 10 mA/cm². (b) Current density ranging from 100 to 500 mA/cm².

allow for this specificity. It is not expected that the Tafel slope is a function of pressure alone because that would indicate a modification of the reaction mechanism steps (Ref. 19). A study examining reactant humidification levels (Ref. 16) has shown Tafel slope to be very dependent on the relative humidity (RH). Although that analysis was performed above 100 °C, it shows that relatively dry gases produce Tafel slopes greater than 100 mV/dec, whereas conditions of more than 60 percent RH can reduce the slope to below 80 mV/dec (Ref. 16). The 7-cell stack incorporates an internal humidification mechanism. The low fitted values are perhaps evidence for satisfactory humidification, but the utilized polarization curve still leaves much uncertainty in precisely determining these slopes.

Unfortunately, the RH in the cells is not precisely known for the reported NFT stack test conditions. Polarization curves were repeated several times over multiple test days, but the effects are not fully defined for variable test conditions leading up to the polarization curves. For example, test durations and load profile varied leading up to initiation of the 2-h load profile. This could alter thermal and hydration profiles from cell to cell and across an active area. It potentially takes 20 to 80 min for membrane electrode assembly (MEA) water content and resistance to equilibrate following changes in potential across the membrane (Refs. 19 and 20).

Although Tafel slope should be independent of pressure, it is possible to observe slight increases with increased pressure (Ref. 21). This is what occurred for both sets of fitted Tafel slopes in this work. Perhaps the fractional water vapor content decrease, as reactant pressure increases, is responsible for this. Alternatively, it could partly be temperature related, providing evidence for inadequate stack thermal control. Suermann measured greater Tafel slopes during long polarization curve step durations (Ref. 19), which was theorized to result from slight variations from thermal equilibrium. Additionally, for this reaction, Tafel slope is theoretically 60 mV/dec, but it can double to 120 mV/dec because of initial oxygen reduction reaction limitations (Ref. 22).

Many sources have experimentally determined or fitted Tafel slope values between 60 and 120 mV/dec. Kim fitted 61 to 63 mV/dec (Ref. 23). Parthasarathy reported 62 to 69 mV/dec at 50 °C with oxygen pressure ranging from 193 to 710 kPa (28 to 103 psia) (Ref. 24). For Xu, oxygen partial pressure, in particular, had no effect on Tafel slope and was determined to be 62 to 65 mV/dec at 100 percent RH and 75 to 79 mV/dec at 50 percent RH, in tests conducted at 80 °C (Ref. 16).

3.3 Resistance R_Ω Discussion

Of comparable published sources with a similar equation format (i.e., in absence of a mass transport term), the Kim et al. fitted resistance values are most similar at 0.345 to 0.391 Ω cm^2 for pure hydrogen-oxygen reactants supplied at 303 kPa (44 psia) and 50 °C (Ref. 23). Interestingly, pressure does not appear to strongly affect R_Ω. The slope of R_Ω versus p is less than that of most of the other observed and fitted parameters. Furthermore, without an exponential mass transport term, the predominant influence to R_Ω may actually be related to intermediate current density mass transport, though including a mass transport term still does not guarantee separation of these given limited data. The commonly used exponential mass transport term also has no direct physical significance (Refs. 11 and 23).

In the intermediate current density region, the cell internal resistance is mainly attributed to the membrane resistance (Ref. 15). Even with polarization curve data comprising hundreds of points that begin to reach the region of mass-transport-limited concentration overpotential, it may not be possible to fully resolve fitted resistance and mass-transport parameters. In fact, Kim et al. describe the fitted multiplier of the exponential mass-transport limitation term as affecting both the linear region of the polarization curve and the high-current transport limitation region. Empirical fit equations simply produce smaller resistance values when including a mass transport term.

In efforts that attempted to better experimentally isolate ohmic overpotential, it was supposed that higher pressure reduces resistance and waste heat generation (Ref. 19). The corresponding improvement was very small as a fraction of total overpotential, even though the studied pressure range was 30 times greater than that in this report. One would therefore expect R_Ω to reflect a minimal observed change in overpotentials over the intermediate current density region, given the narrower pressure range evaluated here. This appears to be the case for both stacks in this report, as the difference in overpotentials is greater at 30 mA/cm^2 than at 300 mA/cm^2 when comparing higher pressure operation to that at lower pressures.

Overall, of the three fitted parameters in this report, ohmic resistance appears to be the most complicated. Many other factors potentially affect R_Ω, including current density, electro-osmotic water drag, and humidification levels of the reactant gas and membrane itself (Ref. 20). Independent of other parameters, the resistance may increase with increasing current density, as was found in Reference 25 when measured after 100 h of operation with pure humified reactants, which is similar to the total operating hours and conditions of the stacks in this work. Thus, one fitted value must represent a parameter that is not constant over the modeled range. When current density in a cell is increased from 0 to 500 mA/cm^2, membrane resistance temporarily increases by about 15 percent (Ref. 25). It is interesting to note that the opposite result may be true for an electrolyzer. Because of improvements in gas phase water transport that result from higher temperatures generated at higher current density, resistance was observed to decrease as a function of current density (Ref. 19). This effect is intensified by the higher operational current densities utilized in electrolyzers.

Even at open circuit the resistance at 60 °C is 15 to 35 percent higher than when measured ex situ, which indicates that the membrane is not fully hydrated under the fuel cell operating conditions, as noted by Büchi and Scherer (Ref. 25) who have speculated that this is a result of thermal changes, electro-osmotic drag, or dry reactant gases. A membrane never returns to the hydration level achieved from liquid water submersion since less hydration is provided from the gas phase.

There is a controversial and complex polymer-water effect, known as Schroeder's paradox, where in materials like

Nafion™, water uptake doubles in liquid water compared with that in saturated vapor conditions (Refs. 26 and 27). This results in a corresponding doubling of the Nafion™ ionic conductivity (Ref. 14). A single empirical fit does not fully represent MEA behavior in mixed-phase conditions, and actual membrane resistance may be lower because of the presence of liquid water on the cathode side. However, it is also possible that this paradox is simply an artifact of sample thermal treatment prior to experimental study (Ref. 28). Thus, in practice, there would be no doubling of water uptake and increase in conductivity from liquid water exposure in this sort of fuel cell.

The Yadav empirical fit equation (Ref. 14) predicts 2 $\Omega \cdot cm^2$ at 138 kPa (20 psia) and 24 $\Omega \cdot cm^2$ at 331 kPa (48 psia) for a 70 °C N117 membrane, assuming Nafion™ is in equilibrium with water vapor. These are much higher than the fitted values and also trend up with increasing pressure, rather than down, since water activity is calculated to decrease. This signifies that either other considerations are more impactful or the membrane is much better humidified than is being assumed. The calculation is also significantly complicated by the likelihood that membrane surface water activity is not in equilibrium with the adjacent vapor (Ref. 20). If Nafion™ were fully hydrated, $a_{H2O} = 1$, then the resistivity is calculated to be 120 $\Omega \cdot cm^2$, which is a fraction of the fitted values but has the correct order of magnitude. Working backwards through Equation (5), the fitted R_Ω values equate to water activity between 0.6 and 0.7.

The resistance at open circuit also depends on the design of the flow field and how reactant gas is supplied. In a design with forced gas convection, Büchi and Scherer found the resistance at 60 °C is substantially higher (210 m$\Omega \cdot cm^2$) than in a design without forced convection (186 m$\Omega \cdot cm^2$) (Ref. 25). Passive NFT stacks do not incorporate any forced convection. It was also determined that it takes approximately 30 s to reach equilibrium at the new resistance level following a change in load. In the current work, cell potential values were obtained following steady operation over similar timescales, though it is probable that internal cell temperatures were elevated during the high-current portions of the current sweeps compared with those nearer the start of that progression. Even though the CTB is generally effective at thermal control of the stacks, it cannot fully eliminate all effects and is not designed to be predictive. Overall, in situ resistance measurements by Büchi and Scherer ranged from 185 to 234 m$\Omega \cdot cm^2$ for hydrogen-oxygen cases, with a tripling of operating pressure having no effect at open circuit and slightly reducing resistance at 500 mA/cm^2. Membrane resistance was more sensitive to current density in scenarios with a parallel flow-field design, similar to the stacks in this report. Perhaps reactant flow improves through the stack internal manifolds and flow fields at higher pressure with this design and without forced convection.

Membrane compression is another factor in overall hydration levels. The membranes in a fuel cell stack of this type are significantly compressed compared with other PEM designs, with pressures approaching 14,000 kPa (2,000 psi). It is known that compression of Nafion™ decreases membrane water content, thus decreasing conductivity (Ref. 29). At lower levels of compression and at RH below 70 percent, this effect accounts for a less than 5 percent change. It is possible that compression limits the overall level of water uptake for these membranes, though it is still believed to provide overall performance benefits. Overall, temperature is a much more impactful input, one that should be carefully controlled when developing and using an empirical modeling equation. Higher temperature also improves the reaction rate, especially at high current densities beyond those evaluated in this work. Careful design is required to balance all factors, and a verified empirical fit equation could clarify these tradeoffs.

Returning to reactant supply pressure, an increase in pressure affects MEA layers in multiple ways. Pressure influences dissolved gas concentrations and oxygen reduction reaction kinetics, with a bearing on mass transport. Higher hydrogen pressure can raise the effective contact area between layers, thus reducing resistance (Ref. 17). It was found that higher pressure on the cathode side produced the opposite effect, though of a much smaller magnitude. Additionally, more pressure can deform MEAs, resulting in porosity and morphology alterations that may either improve or hinder conductivity.

There are practical applications for modeling stack performance and accurately fitting R_Ω. Ohmic resistance tends to increase over the operational life of the stack. The cause of this was isolated to the cathode catalyst layer internal resistance to proton transport (Ref. 30). In a new cell, this particular resistance was only a fraction of the sum of other resistance sources, but it can increase over time to become the major factor in the resistance term. Electrical resistance is likely to be relatively minimal compared with ionic resistance. For a membrane, there is on the order of 1 $\Omega \cdot cm^2$, depending on humidification. Carbon gas diffusion layers have a through-plane resistance of only ~20 m$\Omega \cdot cm^2$ (Ref. 31). Cells assembled without a membrane were observed to exhibit an unmeasurably low resistance (Ref. 25).

Francia et al. noted creep deformation during physical inspection of their test membranes (Ref. 10). These have elsewhere been related to increasing membrane ohmic resistance (Ref. 32). Such degradation could theoretically be monitored through periodic polarization curves and empirical fitting. It is less certain whether this deformation mechanism is a greater factor than catalyst degradation.

There are procedures in operating NFT stacks to prevent cathode degradation. One known mechanism for degradation is localized fuel starvation (Ref. 33). In areas without adequate

hydrogen available for reaction, the current direction can effectively reverse and corrode catalyst support material, resulting in a significantly thinned and poorer performing cell. This can occur when first introducing hydrogen during startup, if air, nitrogen, or oxygen are present on the anode side. Evacuating the stack hydrogen cavity prior to initial pressurization and maintaining adequate hydrogen supply purity should reduce the likelihood of this particular mechanism.

3.4   Additional Considerations

There are many more tradeoffs that influence stack and system design. The stacks are less efficient at lower pressure, producing additional waste heat due to the voltage loss. This heat may or may not be desirable for the system, depending on the environmental conditions. Low pressure also produces higher internal volumetric flow rates since the reactant gases are less dense. It is unknown how this may disturb flow distribution along a manifold or affect cell-to-cell fluid distribution, given a stack designed to operate at a certain pressure and nominal current load. One novel operational concept could be to modulate supply pressure as the current load changes, thus maintaining flow velocity within a desired range. An increased flow rate also reduces residence time in the internal humidifier section of a stack like the 7-cell one, presumably negatively impacting reactant humidification and product water degasification. All of this is simply to acknowledge that fluid flow compromises exist and a more complete treatise should examine these in detail in the future.

3.5   Result Uncertainties

In addition to measurement uncertainty, it is also possible to manipulate the fit parameters so that multiple combinations of parameter values result in similar sum of squared residuals. This potentiality could be mitigated by recording more data points at very low current densities and higher current densities beyond those tested in this project. Such additional information would allow for greater distinction between the various overpotential causes.

Nonuniform current distribution across cells, such as hot spots of high relative current density, could also introduce error in the empirical fit. Cell potentials were calculated as the average of all cells, though there is typically 5 to 10 mV difference between the maximum and minimum cells. This is likely attributable to normal stack construction variance and to temperature profiles across the length of the stack. Cells near

the center of a stack tend to operate at warmer temperatures than end cells that contact endplates of relatively high thermal capacity. Furthermore, actual stack coolant outlet temperature was measured to vary between 59 and 64 °C throughout testing, with temperature highly correlated to current load. No relationship to pressure was found for cell-to-cell potential variance.

The correlations with pressure are based on the supply pressure that is external to the stack. The actual effective pressure is lower at a membrane surface, accounting for lower local pressures related to mass-transport limitations. How much lower is an unknown that is challenging to resolve. Estimating this pressure loss is quite complicated, considering the flow pathway geometries through the manifolds and cell flow fields. Additionally, if the supporting fluidic system cannot sustain consistent supply pressure as current load varies, it could produce an ohmic resistance greater than the true value.

4.0   Conclusions

Various NASA mission concepts necessitate electric power generation from fuel cells operating in nonideal conditions. These adverse situations may include the presence of impurities in the reactant supply, poor or non-existent external gas humidification, or low supply pressures. This study was performed to address concerns related to the reduced operational pressures. Two passive water removal, non-flow-through proton exchange membrane fuel cells were successfully operated on research-grade hydrogen and oxygen reactants supplied at pressures ranging from 310 or 331 kPa (45 or 48 psia) design pressures down to 138 kPa (20 psia).

Even though cell potential decreased with reduced operational pressure, both stacks supported current densities of at least 450 mA/cm^2 at cell potentials greater than 0.6 V in all cases. Polarization curves were fitted with a semi-empirical equation, and the physical principles that influence the fitted parameters were discussed. This showed an increase in effective ohmic resistance and a decrease in reversible cell potential, Tafel slope, and hydrogen crossover current when operating at lower pressures. The low crossover current values determined in this work are likely a result of the relatively few hours of use for these stacks along with limitations in the collected data (i.e., too few test points at low current density). The fitted parameters were compared with theoretical and published values. It was also noted that in this case, Nernst adjustments alone do not predict the entire observed cell potential performance reduction resulting from pressure changes.

Appendix A.—Nomenclature

a_{H_2O} activity of water

b fitted Tafel slope

CTB Common Test Bed

dec decade

E cell potential

E_{adj} adjusted cell potential

E_0 fitted parameter

E_{OCV} open circuit voltage (potential)

E_{ref} reference cell potential

E^0 standard cell potential

F Faraday constant

i current density

i_c crossover current density

l membrane thickness

MEA membrane electrode assembly

NFT non-flow-through

p reactant pressure

p_{adj} adjusted reactant pressure

p_{H_2} hydrogen partial pressure

p_{O_2} oxygen partial pressure

p_{ref} reference reactant pressure

PEM proton exchange membrane

R ideal gas law constant

R_{calc} calculated resistance

R_Ω fitted ohmic resistance

RH relative humidity

T_0 absolute temperature

σ Nafion^{TM} (Chemours Company) conductivity

Appendix B.—Equation (1) Fit to Cell Potential Data

To provide an indication of the fit quality for Equation (1),

$$E = E_{OCV} - b * \log\left(\frac{i + i_c}{i_c}\right) - R_\Omega * i \qquad (1)$$

the average cell potential data points at each tested pressure are compared to the fitted polarization curves for the 12-cell PEM fuel cell stack in Figure B.1 and the 7-cell stack in Figure B.2
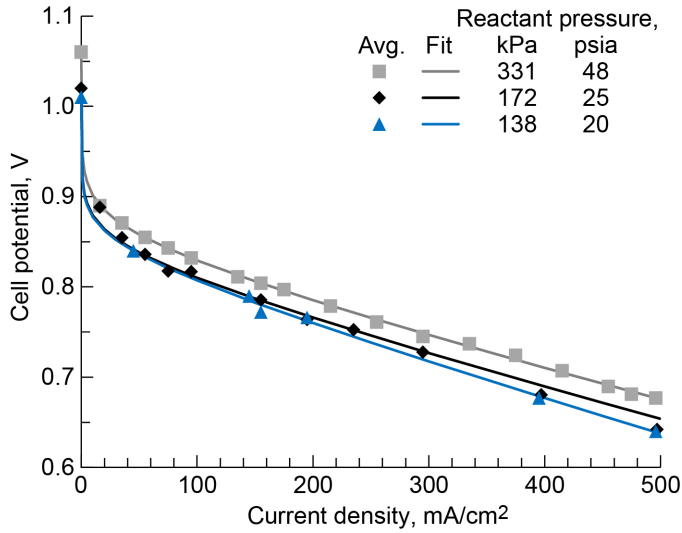

Figure B.1.—Twelve-cell PEM fuel cell stack fitted polarization curves and average cell potential data points at different reactant pressures.
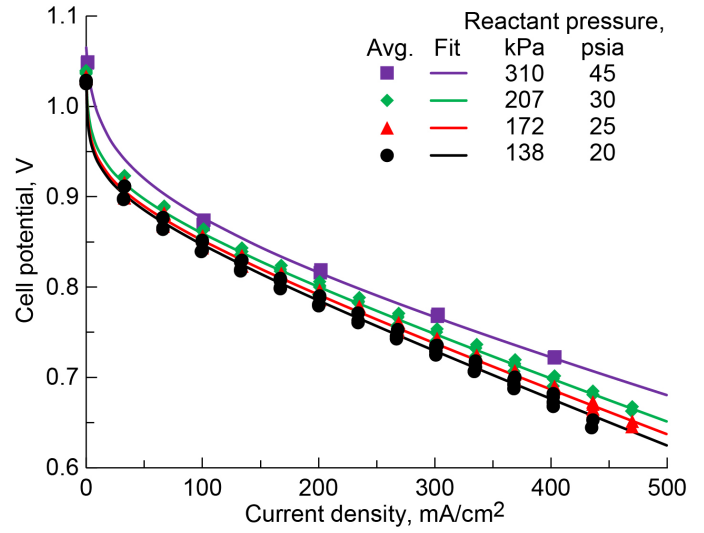

Figure B.2.—Seven-cell PEM fuel cell stack fitted polarization curves and average cell potential data points at different reactant pressures.

References

1. National Aeronautics and Space Administration: NASA Unveils Sustainable Campaign to Return to Moon, on to Mars. 2018. https://www.nasa.gov/feature/nasa-unveils-sustainable-campaign-to-return-to-moon-on-to-mars Accessed March 4, 2021.

2. Polsgrove, Tara; Button, Robert; and Linne, Diane: Altair Lunar Lander Consumables Management. AIAA 2009–6589, 2009.

3. Feasibility of Scavenging Propellants From Lander Descent Stage to Supply Fuel Cells and Life Support. AIAA 2009–6511, 2009.

4. Hoberecht, Mark A.: A Comparison of Flow-Through Versus Non-Flow-Through Proton Exchange Membrane Fuel Cell Systems for NASA's Exploration Missions. NASA/TM—2010-216107, 2010. https://ntrs.nasa.gov

5. Gilligan, Ryan P., et al.: Structural Dynamic Testing Results for Air-Independent Proton Exchange Membrane (PEM) Fuel Cell Technologies for Space Applications. Proceedings of the ASME 2019 International Mechanical Engineering Congress and Exposition, Salt Lake City, UT, 2019.

6. Smith, Phillip J., et al.: Effect of Reactant Purity on Proton Exchange Membrane Fuel Cell Performance. NASA/TP-20215011711, to be published, 2021.

7. Manzo, Michelle A.: NASA Glenn Research Center Electrochemistry Branch Battery and Fuel Cell Development Overview. Presented at the Battelle Energy Storage Roadmap Workshop, Seattle, WA, 2011.

8. Bennett, William R.; Smith, Phillip J.; and Jakupca, Ian J.: Analysis of 100-W Regenerative Fuel Cell Demonstration. NASA/TM-20205000357, 2020. https://ntrs.nasa.gov

9. Vilekar, Saurabh A.; and Datta, Ravindra: The Effect of Hydrogen Crossover on Open-Circuit Voltage in Polymer Electrolyte Membrane Fuel Cells. J. Power Sources, vol. 195, no. 8, 2010, pp. 2241–2247.

10. Francia, Carlotta, et al.: Estimation of Hydrogen Crossover Through Nafion® Membranes in PEMFCs. J. Power Sources, vol. 196, no. 4, 2011, pp. 1833–1839.

11. Hao, Dong, et al.: An Improved Empirical Fuel Cell Polarization Curve Model Based on Review Analysis. Int. J. Chem. Eng., vol. 2016, no. 4109204, 2016.

12. Srinivasan, S.; Hurwitz, H.D.; and Bockris, J. O'M.: Fundamental Equations of Electrochemical Kinetics at Porous Gas-Diffusion Electrodes. J. Chem. Phys., vol. 46, no. 3108, 1967.

13. Barbir, Frano: PEM Fuel Cells: Theory and Practice. Elsevier, Amsterdam, Netherlands, 2005.

14. Yadav, Rameshwar; and Fedkiw, Peter S.: Analysis of EIS Technique and Nafion 117 Conductivity as a Function of Temperature and Relative Humidity. J. Electrochem. Soc., vol. 159, no. 3, 2012, pp. B340–B346.

15. Atifi, Adil; Mounir, Hamid; and El Marjani, Abdellatif: Effect of Internal Currents, Fuel Crossover, and Membrane Thickness on a PEMFC Performance. Proceedings of the International Renewable and Sustainable Energy Conference, Ouarzazate, Morocco, 2014, pp. 907–912.

16. Xu, Hui: Effect of Elevated Temperature and Reduced Relative Humidity on ORR Kinetics for PEM Fuel Cells. J. Electrochemical Society, vol. 152, no. 9, 2005, pp. A1828–A1836.

17. Giner-Sanz, J.J.; Ortega, E.M.; and Perez-Herranz, V.: Hydrogen Crossover and Internal Short-Circuit Currents Experimental Characterization and Modelling in a Proton Exchange Membrane Fuel Cell. Int. J. Hydrog. Energy, vol. 39, no. 25, 2014, pp. 13206–13216.

18. Qin, Y., et al.: Study on the Operating Pressure Effect on the Performance of a Proton Exchange Membrane Fuel Cell Power System. Energ. Convers. Manage., vol. 142, 2017, pp. 357–365.

19. Suermann, Michel; Schmidt, Thomas J.; and Büchi, Felix N.: Cell Performance Determining Parameters in High Pressure Water Electrolysis. Electrochim. Acta, vol. 211, 2016, pp. 989–997.

20. Cheah, May Jean; Kevrekidis, Ioannis G.; and Benziger, Jay: Effect of Interfacial Water Transport Resistance on Coupled Proton and Water Transport Across Nafion. J. Phys. Chem. B, vol. 115, no. 34, 2011, pp. 10239–10250.

21. Mukerjee, Sanjeev; Srinivasan, Supramaniam; and Appleby, A. John: Effect of Sputtered Film of Platinum on Low Platinum Loading Electrodes on Electrode Kinetics of Oxygen Reduction in Proton Exchange Membrane Fuel Cells. Electrochem. Acta, vol. 38, no. 12, 1993, pp. 1661–1669.

22. Holewinski, Adam; and Linic, Suljo: Elementary Mechanisms in Electrocatalysis: Revisiting the ORR Tafel Slope. J. Electrochem. Soc., vol. 159, no. 11, 2012, pp. H864–H870.

23. Kim, Junbom, et al.: Modeling of Proton Exchange Membrane Fuel Cell Performance With an Empirical Equation. J. Electrochem. Soc., vol. 142, 1995, pp. 2670–2674.

24. Parthasarathy, Arvind, et al.: Pressure Dependence of the Oxygen Reduction Reaction at the Platinum Microelectrode/Nafion Interface: Electrode Kinetics and Mass Transport. J. Electrochem. Soc., vol. 139, no. 10, 1992, pp. 2856–2862.

25. Büchi, Felix; Scherer, Gunther G.: In-Situ Resistance Measurements of Nation® 117 Membranes in Polymer

Electrolyte Fuel Cells. J. Electroanal. Chem., vol. 404, no. 1, 1996, pp. 37–43.

26. Weber, Adam; and Kusoglu, Ahmet: Understanding Schroeder's Paradox. Bull. Am. Phys. Soc., vol. 57, no. 1, 2012.

27. Zawodzinski, Thomas A., et al.: Water Uptake by and Transport Through Nafion® 117 Membranes. J. Electrochem. Soc., vol. 140, no. 4, 1993, pp. 1041–1047.

28. Onishi, Lisa M.; Prausnitz, John M.; and Newman, John: Water-Nafion Equilibria. Absence of Schroeder's Paradox. J. Phys. Chem. B, vol. 111, no. 34, 2007, pp. 10166–10173.

29. Kusoglu, Ahmet; Kienitz, Brian; and Weber, Adam Z.: Understanding the Effects of Compression and Constraints on Water Uptake of Fuel-Cell Membranes. J. Electrochem. Soc., vol. 158, no. 12, 2011, pp. B1504–B1514.

30. Park, Sehkyu, et al.: Polarization Losses Under Accelerated Stress Test Using Multiwalled Carbon Nanotube Supported Pt Catalyst in PEM Fuel Cells. J. Electrochem. Soc., vol. 158, no. 3, 2011, pp. B297–B302.

31. Fuel Cells Etc: Gas Diffusion Layer (GDL) Comparison Chart. 2021. https://fuelcellsetc.com/helpful-tools/gas-diffusion-layer-gdl-comparison-chart/ Accessed March 8, 2021.

32. Jao, Ting-Chu, et al.: Degradation on a PTFE/Nafion Membrane Electrode Assembly With Accelerating Degradation Technique. Int. J. Hydrog. Energy, vol. 35, no. 13, 2010, pp. 6941–6949.

33. Meyers, Jeremy; and Darling, Robert M.: Model of Carbon Corrosion in PEM Fuel Cells. J. Electrochem. Soc., vol. 153, 2006, pp. A1432–A1442.